Wall-modeled LES of flow over a Gaussian bump

Prahladh S. Iyer*
National Institute of Aerospace, Hampton, VA 23666

Mujeeb R. Malik†
NASA Langley Research Center, Hampton, VA 23681

We perform wall-modeled large eddy simulations (WMLES) of turbulent flow over a Gaussian-shaped bump geometry, to assess its performance in the acceleration and separation regions of the flow. An unstructured finite-volume solver is used along with an equilibrium wall model. The Mach number of the oncoming flow selected for the simulation is 0.176, and two Reynolds numbers (Re) are simulated that are about 10000 and 36000 based on boundary layer thickness upstream of the bump. Spanwise periodic results for the lower Re case are compared with the available DNS data, while the full three-dimensional simulation results for the higher Re case are compared to available experimental data. Sensitivity of WMLES results are assessed for a number of factors including grid resolution, wall model exchange location, type of wall model, and unstructured grid topology. The WMLES results for the lower Re case agree well with available DNS data in terms of the wall pressure variation, velocity and turbulent stress profile comparisons. The skin-friction predictions show a reduced tendency to separate. This appears to be accentuated for the higher Re case, for the medium resolution grid used in this study, where WMLES does not predict any flow separation in the mean, which is in contrast to the large separation bubble observed in the experiments.

I. Introduction

High fidelity simulation methodologies are required to improve our understanding of flows over complex geometries. Computational Fluid Dynamics (CFD) can play a critical role in the design of aerospace vehicles owing to the detailed information regarding the flow physics and statistics it can provide. Reynolds-averaged Navier-Stokes (RANS)-based methods are currently widely used for high Reynolds number turbulent flows but, in general, are not accurate for complex flows involving separation. High fidelity Direct Numerical Simulation (DNS) and Large Eddy Simulation (LES) methods, while accurate, are infeasible for realistic flight Reynolds number flows. Performing a wall resolved LES simulation of a full powered aircraft configuration in the full flight envelope is a grand challenge problem in the NASA CFD Vision 2030 study [1], which is not expected to be realized in the near-future.

The wall-modeled LES approach, in which the near-wall region is modeled with RANS, while the majority of the length scales away from the wall are resolved using LES, is a reasonable compromise between accuracy and computational cost. Wall-modeled LES can further be classified into (i) stress-based WMLES, and (ii) hybrid RANS/LES methods such as Improved Delayed Detached Eddy Simulation (IDDES). In the stress-based WMLES approach, the computational grid is coarse in the wall-normal and wall-parallel directions, thus requiring the regular no-slip boundary condition to be supplemented by wall shear stress and heat flux/ temperature boundary conditions. See Cabot & Moin [2], Piomelli & Balaras [3], Larsson et al. [4] and Bose & Park [5] for overviews of stress-based WMLES. In IDDES, the grid is very fine in the wall-normal direction but coarse in the wall-parallel direction thus requiring the LES eddy viscosity to be replaced by a RANS eddy viscosity where the majority of the turbulence is modeled. See Spalart [6], Deck [7], Spalart et al. [8] and Shur et al. [9] for an overview of the DES-based approach. In this study, we focus on the stress-based WMLES approach, which is implied when we refer to WMLES in the rest of the paper.

Wall-modeled large eddy simulation (WMLES) and hybrid RANS/LES methods are becoming increasingly popular for high Reynolds number turbulent flow configurations with separation due to their potential to be more accurate compared to Reynolds-averaged Navier-Stokes simulations (RANS), which are the current industry standard. While the RANS technique models all of the turbulence, the WMLES technique resolves a significant portion of the energy-carrying eddies away from the wall. Thus, grid refinement in WMLES is likely to lead to more accurate predictions,

*Research Scientist, AIAA Senior Member.
†Senior Aerodynamicist, Computational AeroSciences Branch, MS 128, AIAA Fellow.

while the modeling error, which dominates in RANS, is independent of the grid resolution. WMLES has shown good promise for a variety of flow configurations involving flow separation [9–29]. Nevertheless, the current framework and models used in WMLES are far from perfect; further understanding and improvements are necessary to enable their use for complex industrial applications [1].

The experimental configuration of the Gaussian bump was proposed by experts at Boeing [30] in order to provide validation data for smooth body flow separation. Some preliminary experiments have been performed by Williams et al. [31] for this configuration. More detailed experiments are being conducted by Boeing and collaborators. We use an unstructured finite-volume solver with the equilibrium wall model to evaluate its performance for the chosen configuration. Most previous WMLES studies involving separation have been restricted to a single Reynolds number (Re), but here, we wish to examine the predictions at two Re, with the smaller one accessible to DNS for detailed comparisons. Uzun & Malik [32] have performed DNS for the same configuration using 2.265 billion grid points with a detailed analysis of the flow physics on the favorable and adverse pressure gradient regions of the flow. Balin et al. [33] have performed IDDES-based WMLES and DNS for this configuration with valuable insights into the flow. Their results indicate that WMLES performance deteriorates as one moves from the favorable to adverse pressure gradient regions of the flow, with larger errors in the separated region of the flow. The stress-based WMLES framework used in the present study has shown promising results in previous studies such as flow over a wall-mounted hump [15], transonic flow past an axisymmetric bump [18], and supersonic flow past a compression ramp[24].

The paper is organized as follows. The details of the flow solver and wall model are briefly discussed in Section II. The flow conditions, configuration, grid and simulation details are discussed in Section III. Assessment of three-dimensional tunnel wall effects using RANS is described in Section IV. WMLES results for the spanwise periodic configuration at $Re_L = 1$ million are discussed in Section V, while three-dimensional and spanwise periodic results for $Re_L = 3.6$ million are discussed in Section VI. A brief summary in Section VII concludes the paper.

II. Numerical Details

The *Charles* solver* is used in the simulations. The compressible solver discretizes the Navier-Stokes equations on unstructured grids using a cell-centered finite-volume methodology. The baseline solver is second-order accurate in space for unstructured grids with an explicit third-order Runge-Kutta time advancement scheme. Numerical stability is achieved by blending with an upwind flux in regions of poor grid quality. Further details about the numerics can be found in Khaligi et al. [34] and Park & Moin [35]. The constant coefficient Vreman model is used to model the subgrid terms with a model coefficient $c = 0.07$ [34, 36], and the equilibrium wall model [37] is used to prescribe the wall shear-stress in this study. The equilibrium wall model is technically only valid for attached regions of the flow as it does not capture nonequilibrium effects in accelerating and separated regions of the flow. Hence, the accuracy of the prediction in nonequilibrium regions is dependent on how much of these effects are captured by the outer layer (resolved by LES) and the grid resolution in the region, and the effect of skin friction on the outer layer in such regions. It uses a mixing-length-based turbulent eddy viscosity in the wall model equations [37]. We have previously used the same setup with the equilibrium wall model to study two-dimensional (in the mean) separated flows [15, 16, 18, 24], and obtained good comparison with available experimental data.

III. Problem Description

The experimental configuration described in Slotnick [30] consists of a symmetric Gaussian-shaped bump in the center of the wind tunnel ($z = 0$) with a length and width L, that extends to the sides of the tunnel ($z/L = \pm 0.5$). It is attached to a flat plate section both upstream and downstream of the bump ($|x/L| > 0.5$), and tapered along the spanwise direction (z) to minimize side-wall interference effects. The shape of the bump can be described by the following equation:

$$y(x,z) = \frac{h_0}{2} e^{-\left(\frac{x}{x_0}\right)^2} \left[1 + \text{erf}\left(\frac{\frac{L}{2} - 2z_0 - |z|}{z_0}\right)\right] \tag{1}$$

Here, x, y and z are the streamwise, wall-normal and spanwise directions of the oncoming boundary layer, and L is the width of the tunnel (which is also equal to the length of the bump). The constants $x_0 = 0.195L$, $z_0 = 0.06L$ and $h_0 = 0.085L$ are used, and the corresponding shape of the bump in the $x - y$ and $y - z$ planes are shown in Figure 1.

*Cascade Technologies, Webpage: `http://www.cascadetechnologies.com` [Last accessed: November 8, 2020]

The term in the square brackets in Equation 1 is unity at $z = 0$, which is used for the spanwise-periodic simulations in this study. Experiments for the speed bump have been carried out by Williams et al. [31] in the Reynolds number ($Re_L = u_\infty L/\nu_\infty$) range of 0.69 – 3.6 million; however, results were reported for $Re_L = 1.3 - 3.5$ million, which corresponds to a freestream Mach number of 0.07 – 0.17. Our simulations are performed at a freestream Mach number of 0.176, and $Re_L = 1$ and 3.6 million. The lower Reynolds number corresponds to the value used by Uzun & Malik [32] in their DNS of this flow configuration, which is used for comparison and validation.

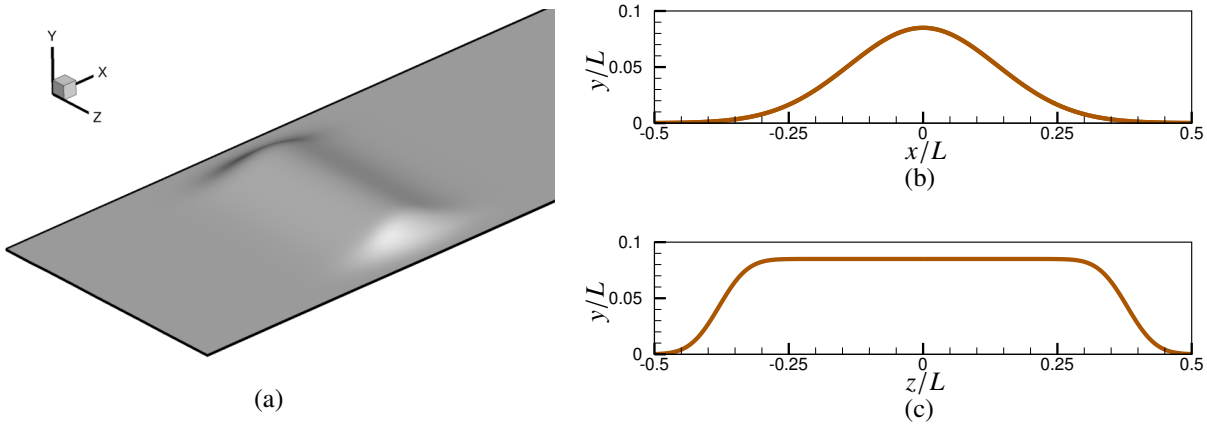

Fig. 1 The shape of the three-dimensional bump (a) in the $x - y$ plane at the symmetry plane $z = 0$ (b), and $y - z$ plane at the center of the bump $x = 0$ (c), are shown.

Most of the WMLES results reported are for the spanwise periodic case, with a spanwise domain width of $L_z/L = 0.04$. The inflow is placed at $x/L = -0.8$, and outflow is at $x/L = 2.0$. Mean flow taken from RANS (see Section IV) using the Spalart-Allmaras (SA) model with rotation and curvature (RC) correction, and the quadratic constitutive relationship for turbulent stress (QCR) is superimposed with synthetic fluctuations using the method of Shur et al. [38], which we have previously used for supersonic shock/turbulence interaction [24, 39] and the NASA juncture flow problem[27]. Sponge boundary conditions (BC) [40] are imposed for $x/L > 1.0$ to minimize reflections from the outflow. The top wall is placed at $y/L = 0.5$ similar to the experiment, but an inviscid slip wall BC is imposed there. For the full 3D simulation, the side walls are also treated as inviscid slip walls. The effect of resolving the viscous tunnel wall boundary layers (top and side walls) appears to be small for the statistics in the symmetry plane based on preliminary RANS simulations (not shown). The equilibrium wall model is applied on the bottom wall with an adiabatic thermal condition. A snapshot of the coarse grid in the symmetry plane is shown in Figure 2.

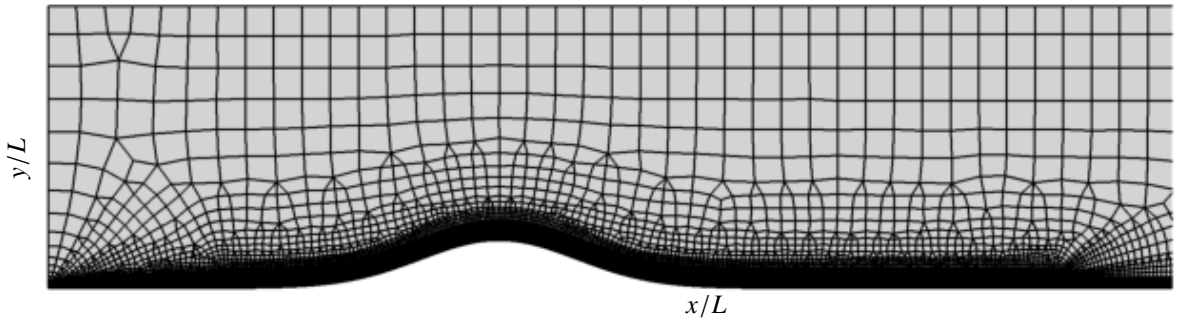

Fig. 2 The coarse grid used in WMLES is shown in the symmetry plane $z = 0$.

The boundary layer thickness of the oncoming turbulent boundary layer (δ_i) is $\approx 0.01L$ at $x/L \approx -0.65$ for $Re_L = 1$ million, which is used as a reference to construct the WMLES grid. Note that the boundary layer thickness varies considerably over the bump, with a value of 0.02 at $x/L = -0.2$ and ≈ 0.04 at $x/L = 0.2$ [32]. Three grids with

varying resolution are used for the spanwise periodic simulations, which are referred to as coarse, medium and fine, respectively. The coarse grid contains about 10 and 8 points per boundary layer thickness (ppd), for $Re_L = 1$ and 3.6 million, respectively, and is mostly isotropic in regions of interest, i.e., $\Delta x = \Delta y = \Delta z$. The grid spacing is $0.001L$ and $0.0005L$ for the coarse and medium grids used here, which contain about 3.4 and 16 million grid points for an $L_z/L = 0.04$. The coarse grid spacing of $0.001L$ corresponds to a viscous wall spacing of $\approx 50 - 100$ and $150 - 300$, for $Re_L = 1$ and 3.6 million, respectively. A finer grid containing 25 million grid points (for $L_z/L = 0.04$) was also used, which reduced the grid spacing by a factor of about 2 over the bump, when compared to the 16 million grid. The minimum wall-normal spacing ($\Delta y_1/L$) is 0.001, 0.00025 and 0.0001 for the coarse, medium and fine grids, while the spanwise spacing is kept constant at 0.001, 0.0005 and 0.0005 for the three grids, respectively. The variation of horizontal grid spacing is compared to the DNS grid (for $Re_L = 1$ million) of Uzun & Malik [32] in Figure 3. The horizontal spacing of the fine 25M grid approaches the DNS value for $Re_L = 1$ million in the adverse pressure gradient region. Note that the spanwise periodic grids used in WMLES are two orders of magnitude coarser than the 2.265 billion grid used in the DNS of Uzun & Malik [32] for the same spanwise extent. The coarse and medium grids for the full 3D configuration whose spacings match the corresponding spanwise periodic grids, contain about 87 and 430 million points, respectively.

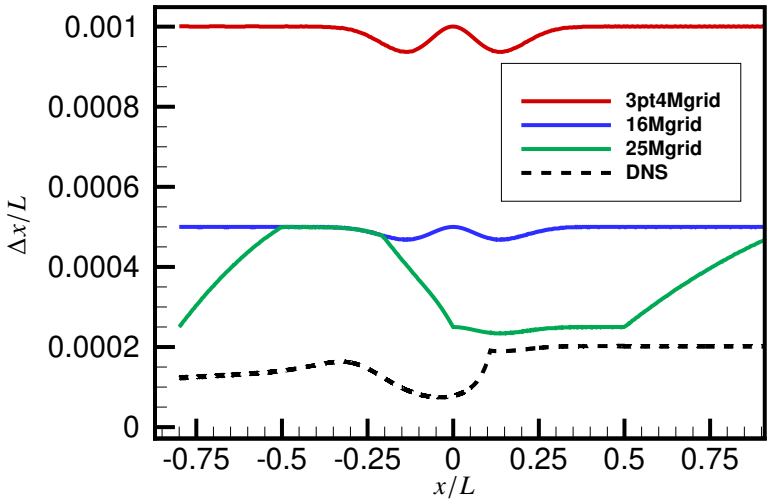

Fig. 3 The horizontal ($x-$direction) grid spacings used in WMLES for the coarse (3.4M), medium (16M) and fine (25M) grids compared to the DNS spacings of Uzun & Malik [32].

Instantaneous vorticity magnitude contours are shown for the coarse spanwise periodic grid at $Re_L = 1$ million in Figure 4 to illustrate the main features of this flow. The upstream turbulent boundary layer first experiences a favorable pressure gradient until the apex of the bump, beyond which it encounters an adverse pressure gradient leading to possible flow separation. Instantaneous isocontours of the $Q-$criterion are shown in Figure 5 for the coarse 87 million grid 3D simulation at $Re_L = 1$ million to depict the vortices captured by the grid resolution. Coherent hairpin eddies are visible upstream, above and downstream of the bump indicating that the outer layer appears to be qualitatively captured by this grid.

IV. Three-dimensional Geometry Effects using RANS

We report RANS calculations for the full 3D configuration, and a 2D slice to evaluate the three-dimensional effects on the flow using the Spalart-Allmaras (SA) turbulence model. We also report the effect of including rotational/curvature (RC) effects in the RANS model, which has a significant effect on this geometry due to the large curvature associated with the bump shape. FUN3D V13.1 [41] is used for these computations. The grid used is wall-resolved with a $\Delta y_w^+ < 1.0$, and a no-slip, isothermal BC is imposed at the wall. All the reported results have residuals converged below 10^{-12}. The no-slip bottom wall begins at $x/L = -1$. The grid is extruded to 1-cell, with spanwise symmetry boundary conditions for the 2D computation. The 2D and 3D grid contains about 0.9 and 21 million cells, respectively. Note that only half the span was simulated for the 3D configuration, due to the inherent symmetry of the problem. The top and

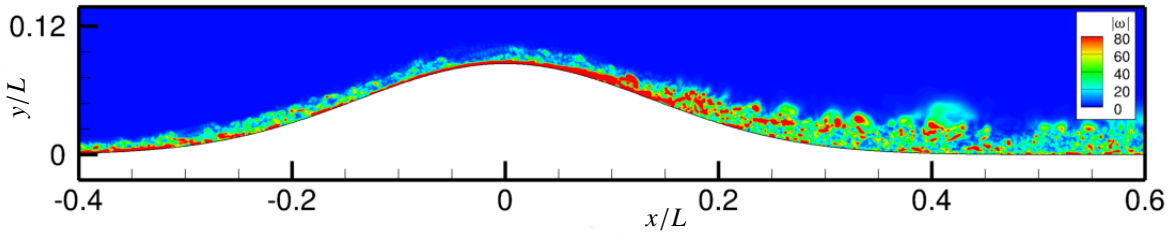

Fig. 4 Instantaneous vorticity magnitude contours ($|\omega|$) are shown for the spanwise periodic coarse WMLES at $Re_L = 1$ million.

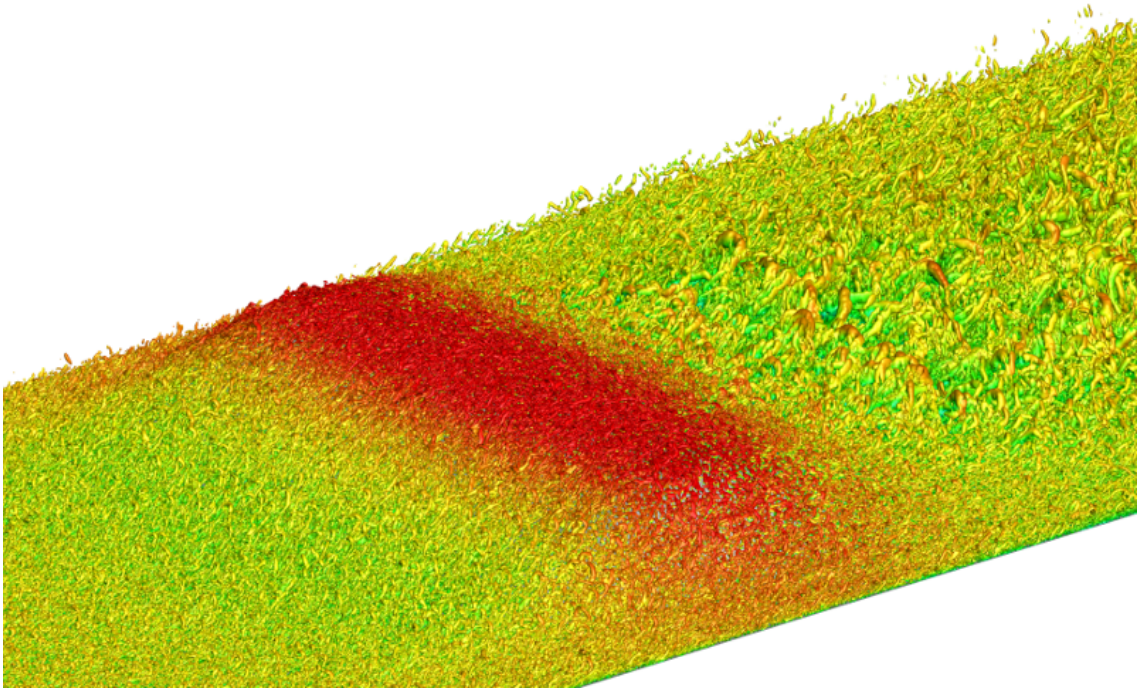

Fig. 5 Isocontours of $Q-$criterion are shown for the 3D coarse grid WMLES at $Re_L = 1$ million to depict the vortical features captured. Turbulent eddies are visible upstream, above and downstream of the bump.

side walls were treated as inviscid slip walls, as preliminary RANS calculations indicated that capturing viscous effects did not have a significant impact on the quantities of interest reported here.

For 3D flows involving separation, the quadratic constitutive relationship (QCR) for the turbulent stress is known to significantly improve the accuracy of predictions [42] for RANS, especially, if the separation is dominated by turbulent stress gradients. Thus, we report results using the regular SA model (linear stress/strain relationship), and the SA-RC-QCR2000 model (QCR with rotation/curvature correction). See the NASA Turbulence Modeling Website[†] for the details of SA-RC-QCR2000 model. The variation of C_f and C_p for the bottom wall in the symmetry plane ($z = 0$) is shown in Figure 6. The effect of 2D versus 3D simulation, and the SA-linear versus SA-RC-QCR2000 model is reported for the two Re_L of 1 and 3.6 million studied here. For the $Re_L = 1$ million case, spanwise periodic DNS results of Uzun & Malik [32] are also shown. The results indicate that for wall quantities of interest in the symmetry plane, the effect of simulating the full 3D configuration is small. However, the SA and SA-RC-QCR2000 predictions show significant differences, with the latter predicting a larger separation bubble. The SA-linear model is closer to the DNS for this case. The 3D simulations also show a reduced C_p magnitude at the apex of the bump due to the decreased blockage compared to the spanwise periodic case, owing to the reduced height of the bump toward the side-walls. Coarse grid WMLES results (not shown) also qualitatively agree with the observations from RANS regarding the effect of simulating the full 3D configuration.

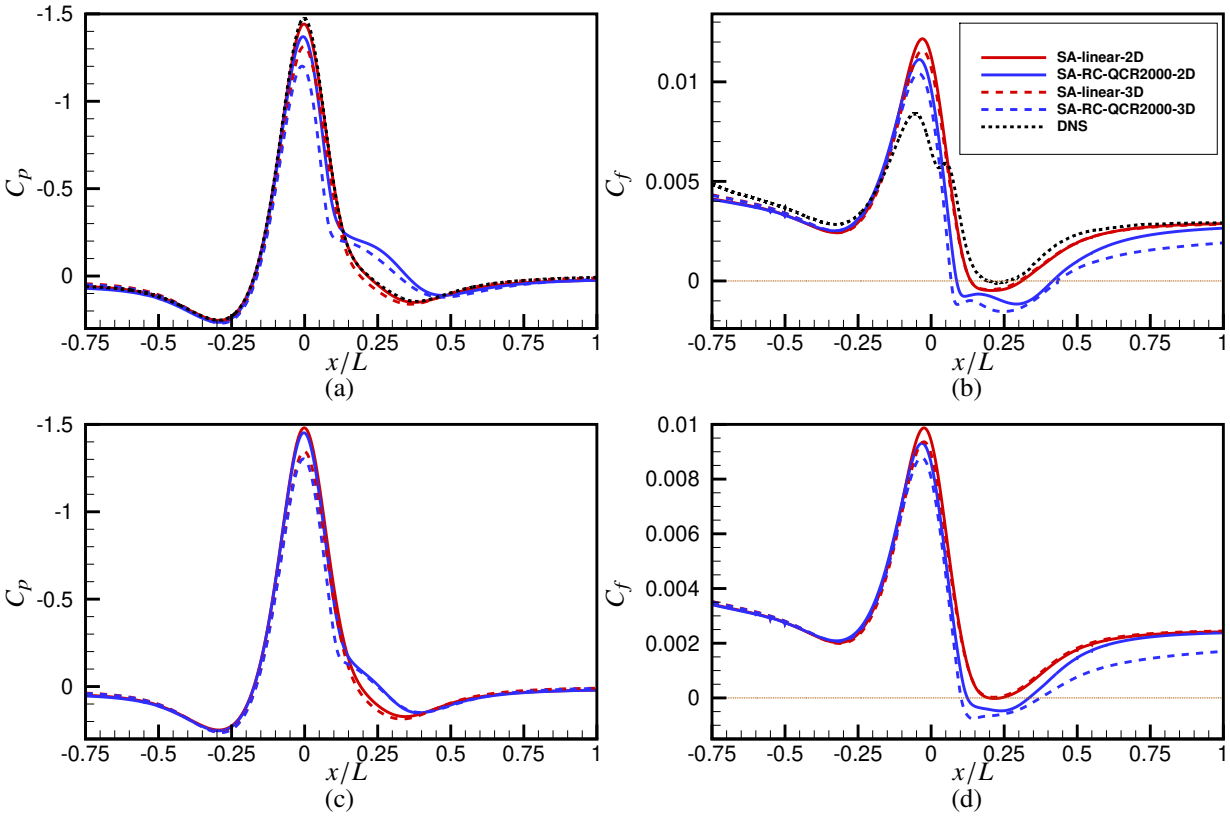

Fig. 6 The variation of wall pressure (a,c) and skin friction (b,d) predicted by SA and SA-RC-QCR2000 RANS models for $Re_L = 1$ million (a,b) and 3.6 million (c,d). The results are reported in the symmetry plane ($z = 0$) for the 3D simulation, and compared to the 2D case. The line legend is shown in Figure (b). The DNS data of Uzun & Malik [32] is used for the lower Reynolds number case.

[†]https://turbmodels.larc.nasa.gov/spalart.html, Last accessed: November 8, 2020

V. $Re_L = 1$ Million Results

We report WMLES results using an equilibrium wall model for $Re_L = 1$ million in this section. We focus on the spanwise periodic results with a spanwise width of $L_z/L = 0.04$, and make detailed comparisons with the DNS data of Uzun & Malik [32]. Unless otherwise specified, the results correspond to the medium 16 million grid.

A. A Priori Analysis using DNS data

We first report a priori analysis of the DNS data to assess the predictive ability of the equilibrium wall model for different exchange locations (EL). The boundary layer thickness (δ) is ≈ 0.01 at $x/L = -0.65$, and so these EL correspond to between 1 and 10% of the upstream δ, which is the typical EL employed in WMLES. Time-averaged velocity and temperature from DNS of Uzun & Malik [32] are input to the wall model, and the wall skin-friction (C_f) output from the wall model are compared to the reference DNS value. The variation of C_f along the bump is shown in Figure 7.

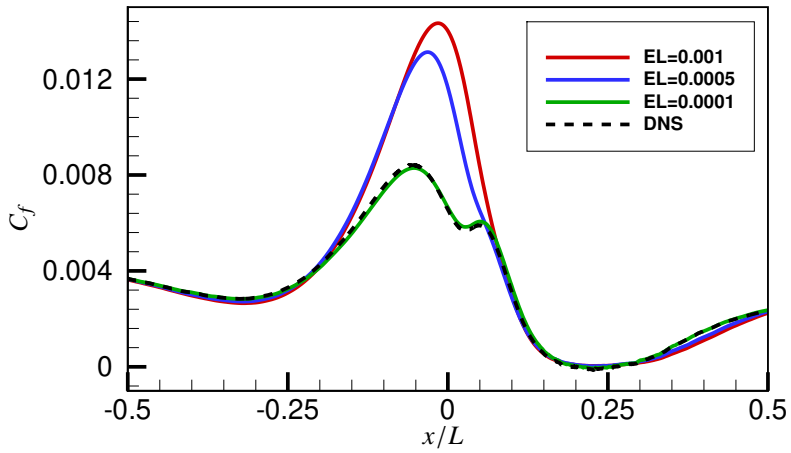

Fig. 7 The skin friction predicted by the equilibrium wall model using the DNS data of Uzun & Malik [32] as input at three different exchange locations.

The results indicate that far upstream of the bump, in the nominally zero-pressure gradient region, the effect of EL is negligible, and shows good agreement with the DNS value. In the accelerating region of the bump $-0.2 < x/L < 0$, there is partial relaminarization of the flow [32, 33], which is not accounted for by the mixing-length-based eddy-viscosity (μ_t) used in the equilibrium wall model. Hence, the larger ELs predict higher C_f since they assume that the flow is fully turbulent similar to the RANS predictions in Figure 6. The $EL = 0.0001L$ predicts accurate C_f since the exchange location lies in the viscous sublayer ($EL^+ < 6.5$) where $\mu_t \approx 0$. Interestingly, all three exchange locations predict nearly identical C_f in the adverse pressure gradient regions ($0 < x/L < 0.3$), and agree well with the DNS value, indicating that the effect of pressure gradient is small for this configuration and Re. Thus, the medium grid was designed with a target EL of 0.0005. Based on the reasoning of Kawai & Larsson [37] that the isotropic eddies should be captured at the EL (i.e., with wall-parallel grid spacing of the order of EL) to minimize log-layer mismatch errors, a grid designed to have an EL of 0.0001 should be finer in each direction by 5X making the total grid over two orders of magnitude larger in size compared to the medium grid.

B. Effect of Grid Resolution

The effect of grid resolution on the wall pressure (C_p) and skin friction (C_f) is shown in Figure 8. The 3.4M, 16M and 25M grid results are shown, with all the grids using an exchange location (EL) of $0.0005L$. The effect of grid resolution on C_p is small, with all grids showing good agreement with the DNS of Uzun & Malik [32]. Some differences are evident in the C_f results, with the finest 25M grid showing the best agreement with DNS. Since the EL falls in the first cell for the coarse grid, some log-layer mismatch is expected here as observed in the upstream C_f comparisons. In the favorable pressure gradient region (-0.25 < x/L < 0), there is an overprediction of C_f for all grids consistent with the a priori analysis. Beyond $x/L > 0$, the coarse grid deviates significantly from DNS, whereas

the medium and fine grids agree well with the DNS, although they have a reduced tendency to separate based on the magnitude of C_f in this region. This is likely due to a posteriori errors from the LES as a priori results agreed better with DNS.

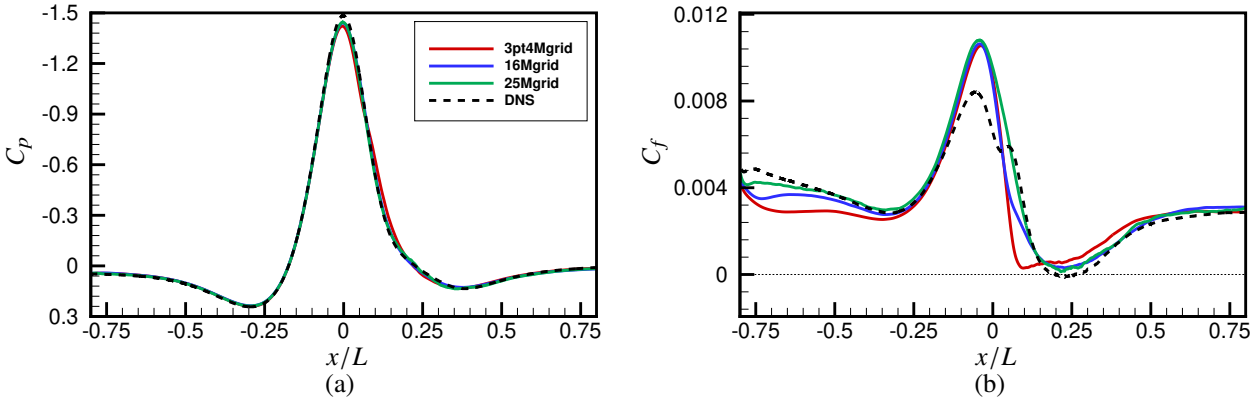

Fig. 8 The variation of wall pressure (a) and skin friction (b) is shown for the $Re_L = 1$ million spanwise periodic WMLES at different grid resolutions with an exchange location (EL) of $0.0005L$. Also included are the DNS result of Uzun & Malik [32].

C. Velocity and Turbulent Stress Comparisons

We report velocity and turbulent stresses from the medium 16M grid WMLES at three horizontal stations corresponding to $x/L = -0.2$, 0 and 0.2 in Figure 9. The DNS results [32] and SA-linear and SA-RC-QCR2000 2D RANS results are also included for comparison. Since the fine 25M grid spacings are closer to DNS, we only report the 16M grid results as these are more representative of WMLES grid resolutions. We only report the resolved stresses as the modeled stresses are small in the outer layer. Also, the WMLES results for $(y - y_w)/L < 0.0005$ should be ignored as these regions are not expected to be captured by the LES grid.

At $x/L = -0.2$, the WMLES result agrees well with DNS in terms of both velocity and stresses. The velocity profile predicted by RANS is in reasonable agreement with DNS, while the stresses deviate significantly from DNS, especially in the inner layer, and do not even qualitatively capture positive values of $\overline{u'v'}$ at this station. At $x/L = 0$, some deviation is observed in the predicted velocity, but the stresses are again significantly better predicted by WMLES compared to RANS. Both RANS models overpredict the peak turbulent shear stress by about 3X, while the WMLES value is very close to DNS. At $x/L = 0.2$, the deviation between WMLES and DNS in terms of both velocity and stresses is larger, likely due to the lower tendency of WMLES to separate. The SA-RC-QCR2000 model predicts separation which causes a large deviation in the velocity at this station, but both the RANS models give worse predictions of stresses when compared to WMLES. Overall, WMLES agrees fairly well with DNS in terms of both velocity and stresses when scaled by the outer units at this Reynolds number. Also, the turbulent stresses are significantly better predicted by WMLES compared to RANS in regions of pressure gradients.

D. Effect of Exchange Location

We report the effect of exchange location for the medium grid in Figure 10. The variation of wall pressure and skin-friction is reported for an EL of 0.000125 and 0.0005. Also included are the DNS [32] and 2D SA-RC-QCR2000 RANS results for comparison. Since an EL of 0.000125 corresponds to the first cell center from the wall, time-filtering was turned on based on the recommendation of Yang et al. [43]. The results indicate that just reducing the EL without appropriately decreasing the wall-parallel spacing (Kawai & Larsson reasoning [37]) does not yield any significant improvement in the results. The time-filtering appears to increase the magnitude of C_f in the upstream attached boundary layer. Varying the time-scale used for the time-filtering did not improve the results.

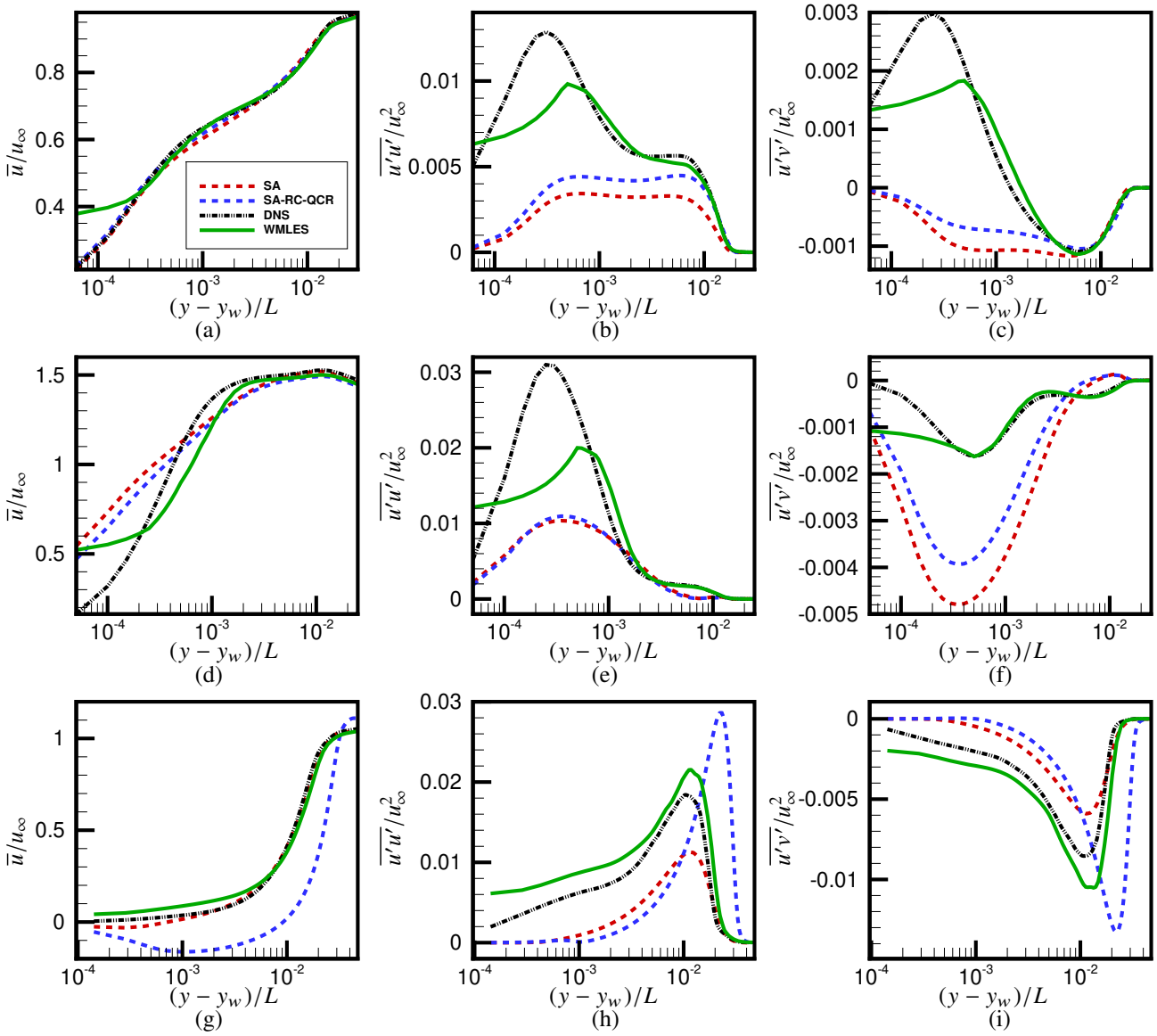

Fig. 9 Profiles of time-averaged velocity ($\overline{u}$), turbulent normal ($\overline{u'u'}$) and shear stress($\overline{u'v'}$) at constant horizontal stations corresponding to $x/L = -0.2$ (a,b,c), 0.0 (d,e,f) and 0.2 (g,h,i) are shown. Note that the top (a,b,c) and bottom (g,h,i) locations correspond to favorable and adverse pressure gradient regions, with the center location corresponding to the center of the bump where the pressure is minimum. Profiles from DNS of Uzun & Malik [32] and RANS are also included for comparison.

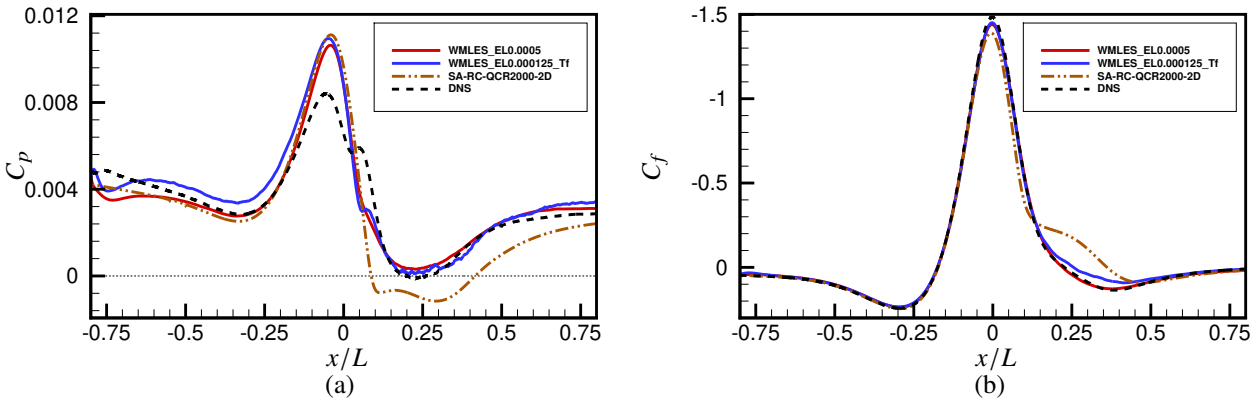

Fig. 10 The variation of wall pressure (a) and skin friction (b) is shown for the $Re_L = 1$ million spanwise periodic WMLES at different exchange locations. Time-filtering is turned on for the lower EL case to minimize log-layer mismatch errors. Also included are the SA-RC-QCR2000 result, and the DNS result of Uzun & Malik [32].

E. Effect of Wall-Model for the Finest Grid

We report the effect of turning off the wall-model for the fine 25M grid used. While the horizontal spacing (Δx) in the adverse pressure gradient region ($0 < x/L < 0.3$) is close to that of DNS (see Figure 3), note that the spanwise and wall-normal spacings are much coarser than DNS. It is of interest to see the extent to which the wall model affects the results. Thus, Figure 11 reports the wall pressure and skin friction variation for the simulations with (WMLES) and without (WRLES) the wall model turned on. Note that WRLES here implies a coarse grid simulation without the wall model, and does not conform to the stringent grid resolution requirements (in all directions) typically employed in literature. The C_f upstream of the bump is much smaller than the DNS value compared to the simulation with wall model. Near the apex of the bump, turning off the wall model improves the C_f predictions, which significantly deteriorate in the adverse pressure gradient regions. C_p predictions in the adverse pressure regions are also worse for the simulation without the wall model. Overall, turning off the wall model makes the results worse, with a decreased tendency to separate.

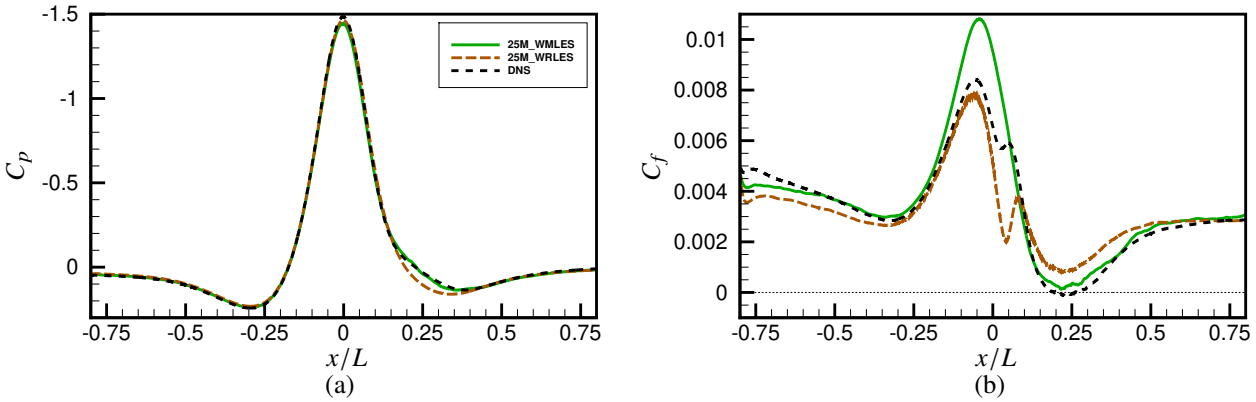

Fig. 11 The variation of wall pressure (a) and skin friction (b) is shown for the $Re_L = 1$ million spanwise periodic WMLES for the fine 25M grid to depict the effect of turning off the wall model. The DNS result of Uzun & Malik [32] are included for comparison.

VI. $Re_L = 3.6$ Million Results

WMLES results for $Re_L = 3.6$ million using the equilibrium wall model are reported in this section. All results use the medium grid with 16 million cells for the spanwise periodic case ($L_z/L = .04$), and 430 million cells for the

three-dimensional configuration. The effect of using the nonequilibium wall model, flat plate DNS solution as inflow, use of polyhedral Voronoi grids, and subgrid scale model are discussed.

A. Three-dimensional Simulation Comparisons

The variation of wall pressure and skin friction in the symmetry plane is shown in Figures 12 (a) and (b). Available experimental data of Williams et al. [31] and RANS data from Section IV are also shown for comparison. The exchange location was set to 0.000125 (first cell-center) for this simulation, and time-filtering was turned off. Our spanwise periodic simulations (not shown) indicated negligible differences between an EL of 0.000125 and 0.0005, and also negligible effect of time-filtering for this Re. No flow separation in the mean is observed in WMLES, while the experiments indicate a large separation bubble between $0.1 < x/L < 0.25$, which causes the wall C_p to flatten in this region. The SA-linear model also does not predict any significant separation, while the SA-RC-QCR2000 model predicts a sizable separation bubble. Note that if one infers the size of separation bubble from the wall C_p comparisons, the SA-RC-QCR2000 model appears to underpredict the size of the separation bubble compared to the experiment. In this case, the WMLES and SA-linear results show good agreement with each other for C_p; however, the peak C_f at the apex of the bump computed by WMLES is lower than that computed by RANS, and larger differences appear in the separation region. Due to the lack of experimental/ DNS data, it is unclear whether the peak C_f predicted by WMLES is more or less accurate than the RANS value. Figure 12 (c) depicts the spanwise variation of wall pressure at $x/L = 0$. Here again, WMLES and SA-linear show good agreement with each other, but deviate from the experiment close to the centerline ($z/L = 0$) as both do not predict separation. The SA-RC-QCR2000 model is closer to experiment at the centerline but does not predict the correct magnitude.

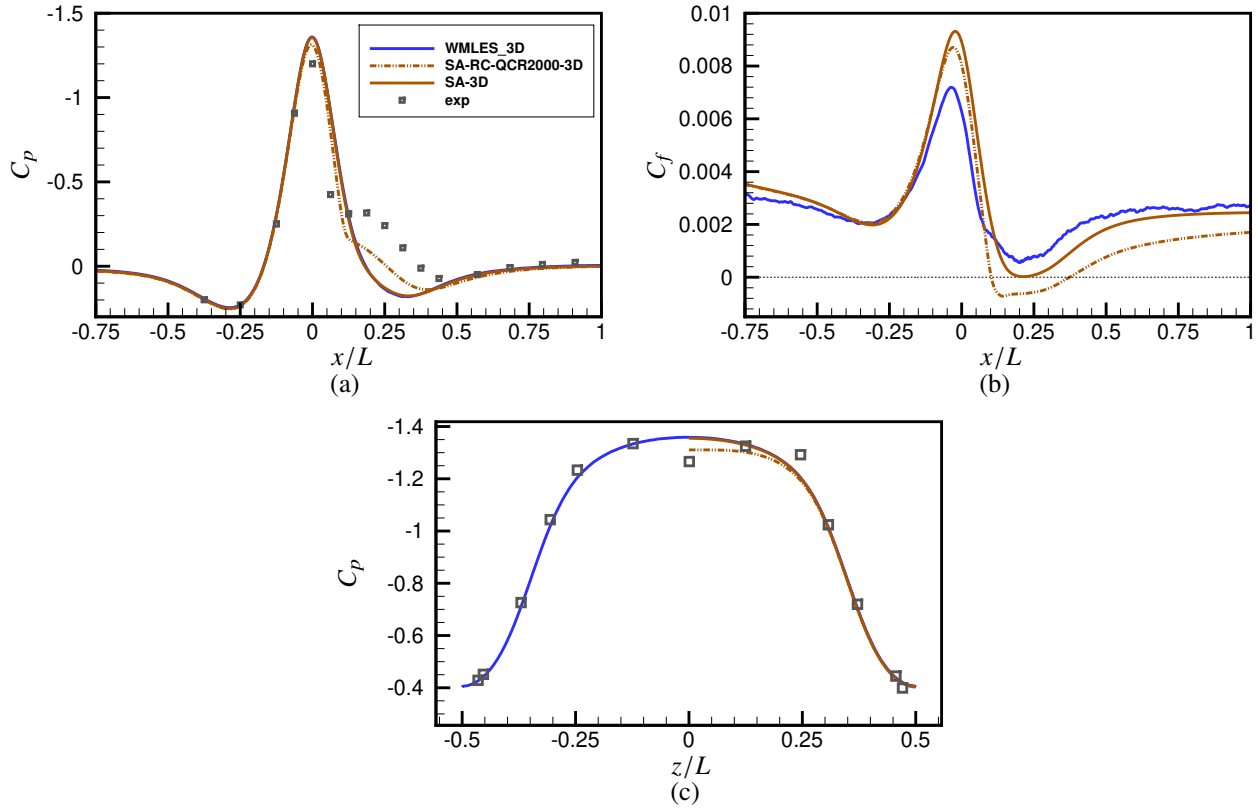

Fig. 12 The variation of wall pressure (a) and skin friction (b) is shown in the symmetry plane ($z = 0$) for the full 3D simulation at $Re_L = 3.6$ million. The spanwise variation of wall pressure at $x/L = 0$ (c) is also shown. The medium grid WMLES (430M) is compared with RANS and experiments of Williams et al.[31].

Figure 13 depicts the wall separation characteristics from the experiment, WMLES and RANS. The oil-flow visualization obtained from the experiments of Williams et al. [31] is shown in (a), while the time-averaged streamlines

are shown for WMLES (b), SA-linear RANS (c) and SA-RC-QCR2000 (d). Contours of the $x-$component of skin friction (C_{fx}) are also shown for all the simulations (b,c,d). Similar to the wall pressure comparisons, the SA-RC-QCR2000 RANS result is qualitatively closest to the experiment. Both the medium 430M grid WMLES and SA-linear RANS results fail to show any flow separation. Grid refinement for WMLES could improve the predictions, but preliminary spanwise-periodic simulations (not shown) indicate that finer grids up to 50M would not change the outcome. Spanwise periodic results with the 25M grid also did not yield any separation in the mean.

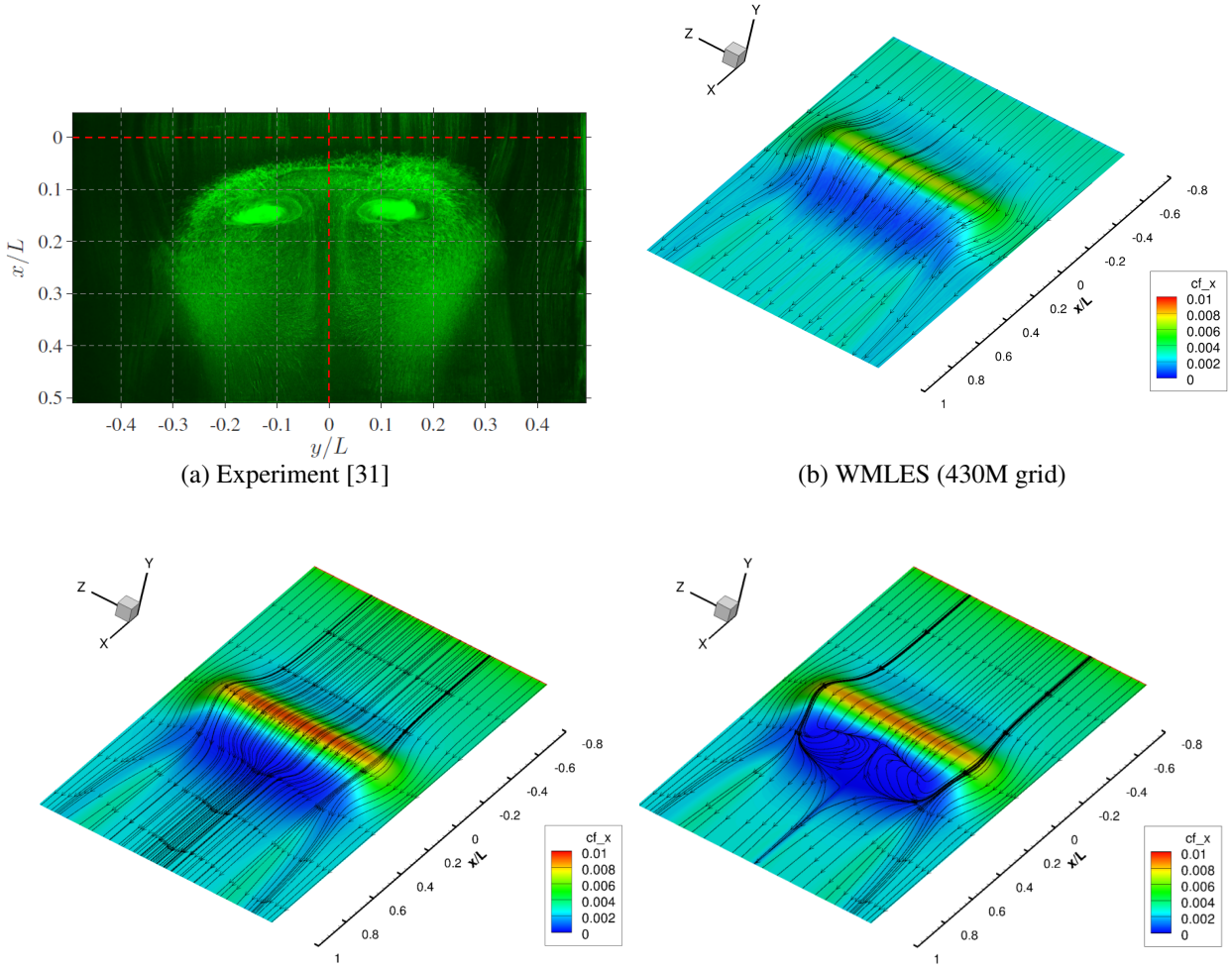

(a) Experiment [31]

(b) WMLES (430M grid)

(c) SA-linear RANS

(d) SA-RC-QCR2000 RANS

Fig. 13 The wall streamlines are shown to depict the separation bubble on the surface of the bump for the 3D configuration. The experimental oil-flow visualization (a) is shown along with time-averaged streamlines from the medium grid WMLES (b). Streamlines from RANS using the SA-linear (c) and SA-RC-QCR2000 (d) models are also shown.

B. Effect of Nonequilibrium Wall Model and Inflow Profile

For all the WMLES results discussed in previous sections, the inflow profile statistics were obtained from the SA-RC-QCR2000 RANS computations. To investigate sensitivity to the inflow mean flow statistics, we perform a simulation using available DNS turbulent flat plate data of Schlatter & Orlu [44]. The DNS flat plate data at $Re_\theta = 2540$ are used as the mean inflow profile at $x/L = -0.67$, which were chosen based on the reported $Re_\theta = 2638$

at $x/L = -0.65$ obtained in the experiments of Williams et al. [31]. We also examine the effect of wall model by performing a simulation using the nonequilibrium wall model of Park & Moin [11]. The medium 16M grid is used with an exchange location of 0.0005, and the simulation is spanwise periodic with a span of $L_z/L = 0.04$. Figure 14 shows the variation of wall pressure and skin-friction. The results indicate that the inflow profile used, and the nonequilibrium wall model have negligible effect on the wall pressure. The nonequilibrium wall model yields a higher peak in C_f near the apex of the bump, with some differences in C_f around $x/L \approx 0.1$, but overall does not produce larger flow separation. Thus, it appears that the absence of separation at this Re may be due to errors in the LES solution.

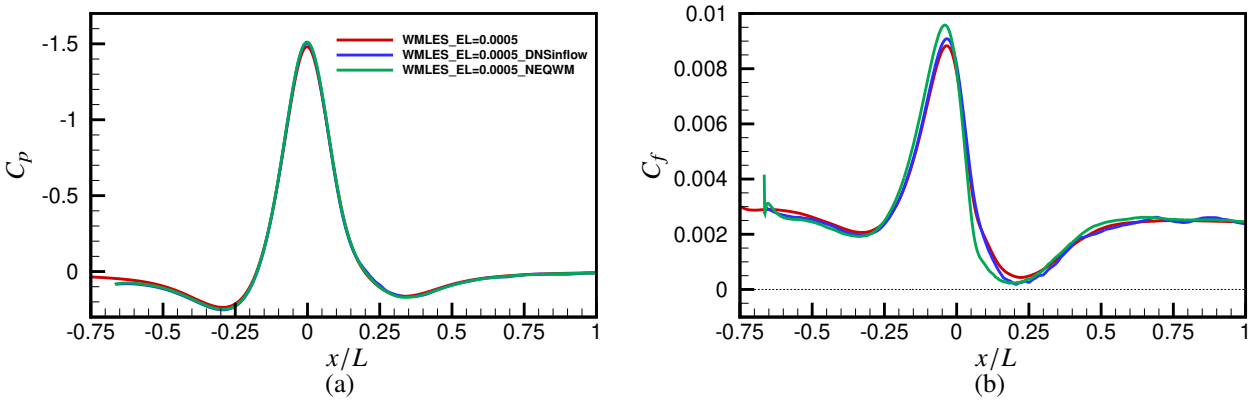

Fig. 14 The variation of wall pressure (a) and skin-friction (b) is shown for the $Re_L = 3.6$ million spanwise periodic WMLES. The effect of inflow profile for the equilibrium wall model is shown, along with the effect of nonequilibrium wall model.

C. Effect of Voronoi Grid

Thus far, all the WMLES results used a hex-dominant unstructured mesh generated using *Pointwise V18.3* [‡]. To investigate the effect of mesh topology, we use a polyhedral Voronoi grid generated using the *Charles V19.3.0* [§] tool called *Stitch*. A snapshot of the unstructured and polyhedral Voronoi grids is shown in Figure 15. The polyhedral Voronoi solver uses the first grid point as the exchange location, and an algebraic wall model is used instead of solving the full equilibrium wall model equations. The differences between the algebraic and the full equilibrium wall model are negligible for subsonic flows such as the present case. The polyhedral grid is isotropic in refinement regions specified by the user. We use three refinement regions each extending a width of $0.01L$, and doubling in grid size with increasing distance from the wall. The near-wall refinement region had an input grid size of $0.0005L$, while the actual size of the final grid was $0.00043L$. The background grid size is coarser by a factor of 2^3, and is 0.0034. The Voronoi grid contains about 14.5 million cells. The inflow of the Voronoi grid was placed at $x/L = -0.67$, and the flat plate DNS solution used in Section VI.B was used as the inflow mean profile. Synthetic inflow turbulence was generated using a digital-filtering-based strategy.

The variation of wall pressure and skin friction are compared between the medium 16M unstructured grid with inflow at $x/L = -0.8$, and the polyhedral Voronoi grid at $x/L = -0.67$ in Figures 16 (a) and (b). Note that the results of the Voronoi grid are not averaged along the span in these results, which explains some lack of smoothness in the skin-friction variation. Also, the surface Voronoi results were interpolated onto a line for a one-to-one comparison. Overall, the results indicate minimal differences between the two grids in terms of the C_p and C_f predictions. Some differences are observed in C_f at $x/L \approx 0.1$, which could be due to the different EL used in the two cases. We also performed a Voronoi grid simulation using random roughness to trip the flow to turbulence with inflow at $x/L = -1.2$. The viscous no-slip boundary condition was imposed between $-1 < x/L < -0.76$, where the flow is expected to be laminar. In the experiments of Williams et al. [31], 240-grit sand paper roughness was used to trip the flow to turbulence. Thus, the surface nodes were perturbed randomly by $5.5x10^{-5}L$ between $-0.76 < x/L < -0.73$ to trip the flow to turbulence. The wall model was turned on at the beginning of the trip. The results for the random roughness trip case is shown in Figures 16 (c) and (d). The C_f variation indicates that the flow trips to turbulence by $x/L \approx -0.5$, and

[‡]Pointwise, Inc., Webpage: `http://www.pointwise.com` [Last accessed: November 8, 2020]

[§]Cascade Technologies, Webpage: `http://www.cascadetechnologies.com` [Last accessed: November 8, 2020]

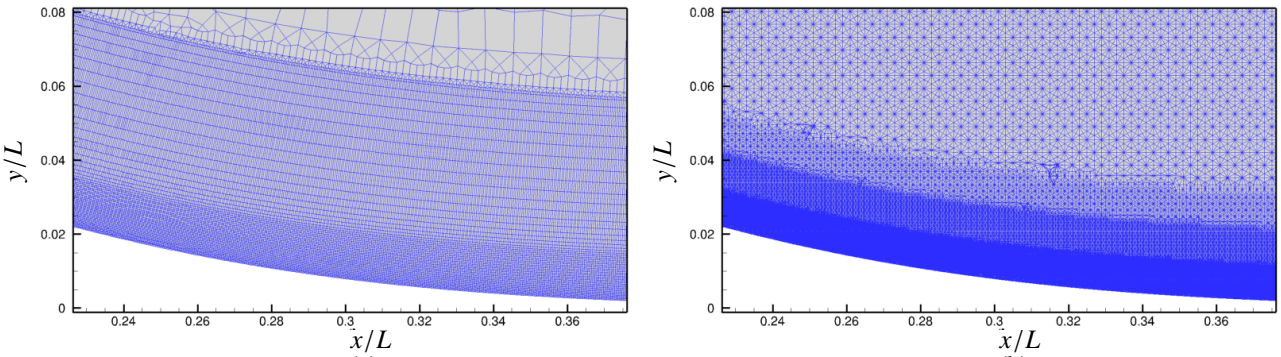

Fig. 15 The medium (16M) hex-dominant unstructured grid generated using *Pointwise V18.3* (a), and the Voronoi polyhedral grid generated using the *Charles* Stitch utility (b) with similar near-wall resolution of $0.0005L$ are shown.

the C_f is slightly overpredicted upstream of the bump compared to the value obtained using the unstructured grid and synthetic inflow turbulence. In terms of the C_p and C_f predictions over the bump, the simulations with the trip yields qualitatively similar results to the Voronoi grid with synthetic inflow turbulence in Figures 16 (a) and (b). These results indicate that the synthetic inflow turbulence is not responsible for the lack of separation over the bump.

D. Effect of Subgrid Scale Model

We use the polyhedral Voronoi grid and solver used in Section VI.C to assess the effect of subgrid scale model on the flow. We compare the constant coefficient Vreman model with a local Dynamic Smagorinsky model (DSM). The DSM model as implemented in *Charles 19.3.0* performs local time-averaging over a time-scale equal to the inverse strain-rate magnitude for numerical stability. The variation of wall pressure and skin friction are shown in Figure 17. While the differences in wall pressure are negligible, some minor differences are seen in the skin-friction variation at $x/L \approx 0.1$. Overall, no significant change in the tendency to separate is observed between the Vreman and DSM subgrid scale models for the present grid and flow conditions.

VII. Summary

We performed wall-modeled large eddy simulations (WMLES) of the flow past a Gaussian bump at Reynolds numbers of 1 and 3.6 million based on the length of the bump. Reynolds-averaged Navier-Stokes (RANS) simulations indicated that the symmetry-plane results of the full three-dimensional configuration did not differ significantly from a two-dimensional simulation carried out in the symmetry plane. Hence, we focused on the spanwise periodic simulation for the $Re_L = 1$ million flow, since detailed DNS data were available for comparison. The effect of grid resolution, exchange location and turning off the wall-model was assessed by comparison with DNS data. Overall, the medium and fine grids yielded good agreement with DNS of Uzun & Malik [32]. The velocity and stress predicted by WMLES were significantly better than SA and SA-RC-QCR2000 RANS models. The skin-friction variation predictions by WMLES in the adverse pressure gradient region indicated a slightly decreased tendency to separate when compared to DNS. For the higher $Re_L = 3.6$ million case, full three-dimensional simulation results using the medium 430 million grid was compared to the experiments of Williams et al. [31]. WMLES results did not show any flow separation in the mean, in contrast to the experiment. The SA-RC-QCR2000 RANS model predicted a separation bubble size closest to the experiment compared to SA RANS and WMLES; however, it overpredicted separation at $Re_L = 1$ million compared to the DNS data. The effect of inflow profile, and that of nonequilibrium wall model were small on the WMLES results. Finally, the effects of grid topology and subgrid scale model were examined using polyhedral Voronoi grids, which also did not significantly change the results. Future work will include performing finer-grid simulations, and investigating possible reasons for lack of separation in WMLES for the higher Re flow.

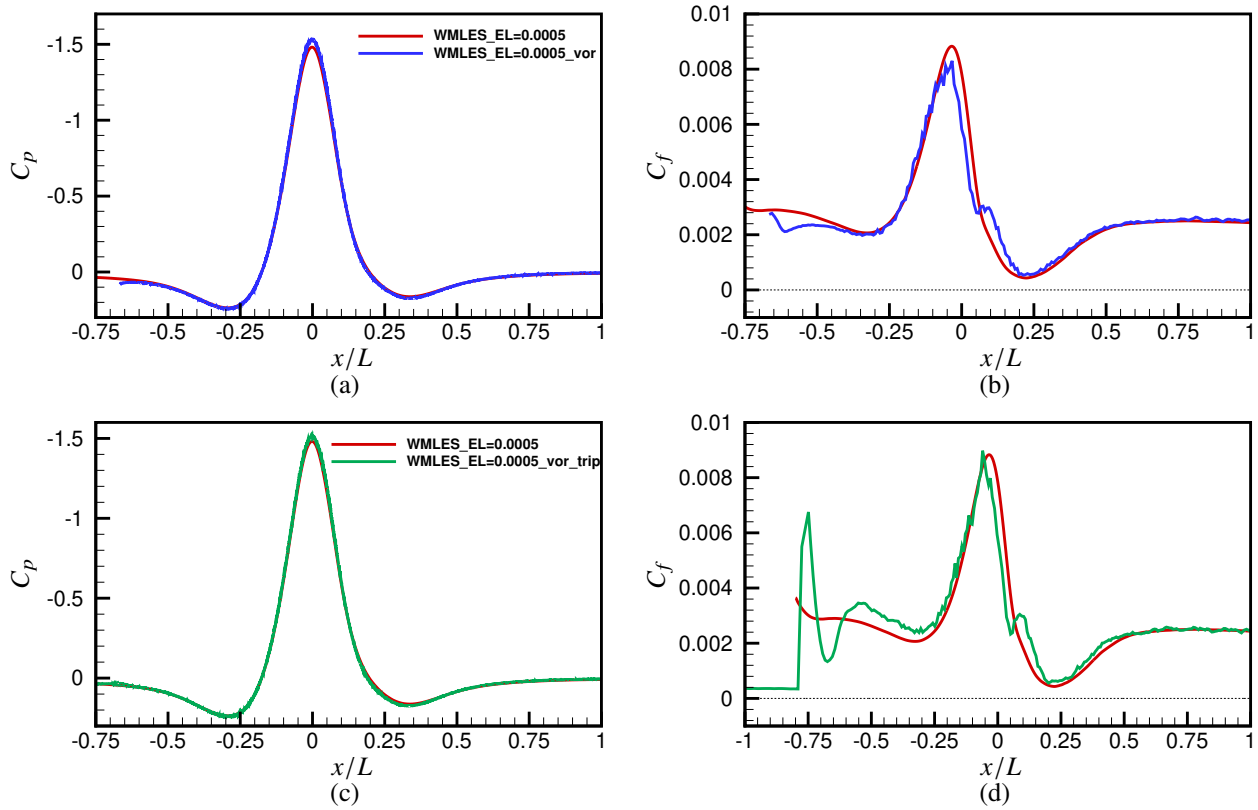

Fig. 16 The variation of wall pressure (a,c) and skin friction (b,d) is shown for the $Re_L = 3.6$ million spanwise periodic WMLES using the hex-dominant unstructured grid and the polyhedral Voronoi grid. The Voronoi results using synthetic inflow turbulence (a,b), and random roughness trip (c,d) are shown. Note that the results from the Voronoi grid are not spanwise averaged, and hence less smooth when compared to the hex-dominant unstructured grid.

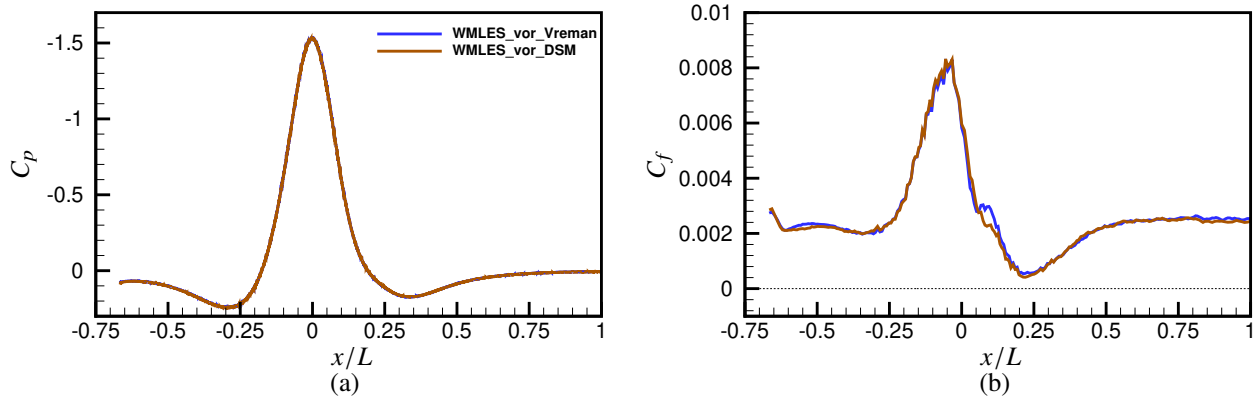

Fig. 17 The variation of wall pressure (a) and skin friction (b) is shown for the $Re_L = 3.6$ million spanwise periodic WMLES using the polyhedral Voronoi grid. The effect of subgrid scale model is shown.

Acknowledgments

This research is sponsored by the NASA Transformational Tools and Technologies (TTT) Project of the Transformative Aeronautics Concepts Program under the Aeronautics Research Mission Directorate. The work of the first author was sponsored by NASA under cooperative agreement NNL09AA00A. We thank Cascade Technologies for providing the Charles solver and consultation in use of the code, and Dr. Ali Uzun for providing the DNS data and for useful discussions. Computational resources supporting this work were provided by the NASA High-End Computing (HEC) Program through the NASA Advanced Supercomputing (NAS) Division at Ames Research Center. Finally, we thank Ali Uzun, Kyle Anderson and Steven Bauer for comments on the manuscript.

References

[1] Slotnick, J., Khodadoust, A., Alonso, J., Darmofal, D., Gropp, W., Lurie, E., and Mavriplis, D., "CFD vision 2030 study: a path to revolutionary computational aerosciences," NASA-CR-2014-218178, 2014.

[2] Cabot, W., and Moin, P., "Approximate wall boundary conditions in the large-eddy simulation of high Reynolds number flow," *Flow, Turbulence and Combustion*, Vol. 63, No. 1–4, 2000, pp. 269–291.

[3] Piomelli, U., and Balaras, E., "Wall-layer models for large-eddy simulations," *Annual Review of Fluid Mechanics*, Vol. 34, No. 1, 2002, pp. 349–374.

[4] Larsson, J., Kawai, S., Bodart, J., and Bermejo-Moreno, I., "Large eddy simulation with modeled wall-stress: recent progress and future directions," *Mechanical Engineering Reviews*, Vol. 3, No. 1, 2016, pp. 15–00418.

[5] Bose, S. T., and Park, G. I., "Wall-modeled large-eddy simulation for complex turbulent flows," *Annual Review of Fluid Mechanics*, Vol. 50, No. 1, 2018.

[6] Spalart, P. R., "Detached-eddy simulation," *Annual Review of Fluid Mechanics*, Vol. 41, 2009, pp. 181–202.

[7] Deck, S., "Zonal-detached-eddy simulation of the flow around a high-lift configuration," *AIAA journal*, Vol. 43, No. 11, 2005, pp. 2372–2384.

[8] Spalart, P. R., Deck, S., Shur, M., Squires, K., Strelets, M. K., and Travin, A., "A new version of detached-eddy simulation, resistant to ambiguous grid densities," *Theoretical and computational fluid dynamics*, Vol. 20, No. 3, 2006, pp. 181–195.

[9] Shur, M. L., Spalart, P. R., Strelets, M. K., and Travin, A. K., "A hybrid RANS-LES approach with delayed-DES and wall-modelled LES capabilities," *International Journal of Heat and Fluid Flow*, Vol. 29, No. 6, 2008, pp. 1638–1649.

[10] Balakumar, P., Park, G., and Pierce, B., "DNS, LES, and wall-modeled LES of separating flow over periodic hills," *Proceedings of the Summer Program, Center for Turbulence Research, Stanford University*, 2014, pp. 407–415.

[11] Park, G. I., and Moin, P., "An improved dynamic non-equilibrium wall-model for large eddy simulation," *Physics of Fluids*, Vol. 26, No. 1, 2014, p. 015108.

[12] Bermejo-Moreno, I., Campo, L., Larsson, J., Bodart, J., Helmer, D., and Eaton, J. K., "Confinement effects in shock wave/turbulent boundary layer interactions through wall-modelled large-eddy simulations," *Journal of Fluid Mechanics*, Vol. 758, 2014, pp. 5–62.

[13] Yang, X., Sadique, J., Mittal, R., and Meneveau, C., "Integral wall model for large eddy simulations of wall-bounded turbulent flows," *Physics of Fluids*, Vol. 27, No. 2, 2015, p. 025112.

[14] Duda, B., and Fares, E., "Application of a Lattice-Boltzmann method to the separated flow over the NASA hump," AIAA Paper 2016–1836, 2016.

[15] Iyer, P. S., and Malik, M. R., "Wall–modeled large eddy simulation of flow over a wall–mounted hump," AIAA Paper 2016–3186, 2016.

[16] Iyer, P. S., Park, G. I., and Malik, M. R., "A comparative study of wall models for LES of turbulent separated flow," Proceedings of the 2016 Summer Program, Center for Turbulence Research, Stanford University, 2016.

[17] Park, G. I., "Wall-modeled large-eddy simulation of a high Reynolds number separating and reattaching flow," *AIAA Journal*, 2017, pp. 3709–3721.

[18] Iyer, P. S., Park, G. I., and Malik, M. R., "Wall–modeled large eddy simulation of transonic flow over an axisymmetric bump with shock-induced separation," AIAA Paper 2017-3953, 2017.

[19] Gritskevich, M., Garbaruk, A., and Menter, F., "A comprehensive study of improved delayed detached eddy simulation with wall functions," *Flow, Turbulence and Combustion*, Vol. 98, No. 2, 2017, pp. 461–479.

[20] Fukushima, Y., and Kawai, S., "Wall-modeled large-eddy simulation of transonic airfoil buffet at high Reynolds number," *AIAA Journal*, Vol. 56, No. 6, 2018, pp. 2372–2388.

[21] Kiris, C. C., Stich, D., Housman, J. A., Kocheemoolayil, J. G., Barad, M. F., and Cadieux, F., "Application of Lattice Boltzmann and Navier-Stokes methods to NASA's wall mounted hump," AIAA Paper 2018-3855, 2018.

[22] Mettu, B. R., and Subbareddy, P. K., "Wall modeled LES of compressible flows at non-equilibrium conditions," AIAA Paper 2018-3405, 2018.

[23] Gonzalez, D. R., Adler, M. C., and Gaitonde, D. V., "Large-eddy simulation of compressible flows with an analytic non-equilibrium wall model," AIAA Paper 2018-0835, 2018.

[24] Iyer, P. S., and Malik, M. R., "Large-eddy simulation of axisymmetric compression corner flow," AIAA Paper 2018-4031, 2018.

[25] Mettu, B. R., and Subbareddy, P. K., "Modeling non-equilibrium effects in wall modeled LES of high-speed flows," AIAA Paper 2019-3699, 2019.

[26] Gao, W., Zhang, W., Cheng, W., and Samtaney, R., "Wall-modelled large-eddy simulation of turbulent flow past airfoils," *Journal of Fluid Mechanics*, Vol. 873, 2019, pp. 174–210.

[27] Iyer, P. S., and Malik, M. R., "Wall-modeled LES of the NASA juncture flow experiment," AIAA Paper 2020-1307, 2020.

[28] Lozano-Duran, A., Bose, S. T., and Moin, P., "Prediction of trailing edge separation on the NASA Juncture Flow using wall-modeled LES," AIAA Paper 2020-1776, 2020.

[29] Ghate, A. S., Housman, J. A., Stich, G.-D., Kenway, G., and Kiris, C. C., "Scale resolving simulations of the NASA Juncture Flow Model using the LAVA solver," AIAA Paper 2020-2735, 2020.

[30] Slotnick, J. P., "Integrated CFD validation experiments for prediction of turbulent separated flows for subsonic transport aircraft," NATO Science and Technology Organization, Meeting Proceedings RDP, STO-MP-AVT-307, 2019.

[31] Williams, O., Samuell, M., Sarwas, E. S., Robbins, M., and Ferrante, A., "Experimental study of a CFD validation test case for turbulent separated flows," AIAA Paper 2020-0092, 2020.

[32] Uzun, A., and Malik, M. R., "Simulation of a turbulent flow subjected to favorable and adverse pressure gradients," AIAA Paper 2020-3061, 2020.

[33] Balin, R., Jansen, K. E., and Spalart, P. R., "Wall-Modeled LES of flow over a Gaussian bump with strong pressure gradients and separation," AIAA Paper 2020-3012, 2020.

[34] Khalighi, Y., Ham, F., Nichols, J., Lele, S., and Moin, P., "Unstructured large eddy simulation for prediction of noise issued from turbulent jets in various configurations," AIAA Paper 2011-2886, 2011.

[35] Park, G. I., and Moin, P., "Numerical aspects and implementation of a two-layer zonal wall model for LES of compressible turbulent flows on unstructured meshes," *Journal of Computational Physics*, Vol. 305, 2016, pp. 589–603.

[36] Vreman, A., "An eddy-viscosity subgrid-scale model for turbulent shear flow: Algebraic theory and applications," *Physics of fluids*, Vol. 16, No. 10, 2004, pp. 3670–3681.

[37] Kawai, S., and Larsson, J., "Wall-modeling in large eddy simulation: length scales, grid resolution, and accuracy," *Physics of Fluids (1994-present)*, Vol. 24, No. 1, 2012, p. 015105.

[38] Shur, M. L., Spalart, P. R., Strelets, M. K., and Travin, A. K., "Synthetic turbulence generators for RANS-LES interfaces in zonal simulations of aerodynamic and aeroacoustic problems," *Flow, Turbulence and Combustion*, Vol. 93, No. 1, 2014, pp. 63–92.

[39] Iyer, P. S., and Malik, M. R., "Analysis of the equilibrium wall model for high-speed turbulent flows," *Physical Review Fluids*, Vol. 4, No. 7, 2019, p. 074604.

[40] Freund, J. B., "Proposed inflow/outflow boundary condition for direct computation of aerodynamic sound," *AIAA journal*, Vol. 35, No. 4, 1997, pp. 740–742.

[41] Biedron, R. T., Carlson, J. R., Joseph, M. D., Gnoffo, P. A., Hammond, D. P., Jones, W. T., Kleb, B., Lee-Rausch, E. M., Nielsen, E. J., Park, M. A., Rumsey, C. L., Thomas, J. L., and Wood, W. A., "FUN3D manual: 13.1," NASA-TM-2019580, 2017.

[42] Spalart, P. R., "Strategies for turbulence modelling and simulations," *International Journal of Heat and Fluid Flow*, Vol. 21, No. 3, 2000, pp. 252–263.

[43] Yang, X. I., Park, G. I., and Moin, P., "Log-layer mismatch and modeling of the fluctuating wall stress in wall-modeled large-eddy simulations," *Physical Review Fluids*, Vol. 2, No. 10, 2017, p. 104601.

[44] Schlatter, P., and Örlü, R., "Assessment of direct numerical simulation data of turbulent boundary layers," *Journal of Fluid Mechanics*, Vol. 659, 2010, p. 116.